Numerical Investigation of Plasma-Based Control for Low-Reynolds-Number Airfoil Flows

Donald P. Rizzetta* and Miguel R. Visbal†

U.S. Air Force Research Laboratory, Wright-Patterson Air Force Base, Ohio 45433-7512

    Large-eddy simulations are carried out to investigate the use of plasma-based actuation for the control of flows over a finite span wing at low Reynolds numbers. The wing section corresponds to the SD7003 airfoil, which is representative of those employed for micro air vehicle applications. Dielectric-barrier-discharge plasma actuators are used to modify the transitional flow and improve aerodynamic performance. Solutions are obtained to the Navier–Stokes equations, which were augmented by source terms used to represent plasma-induced body forces imparted by the actuators on the fluid. Simple phenomenological models provided the body forces generated by the electric field of the plasma surrounding the actuators. The numerical method is based upon a high-fidelity time-implicit scheme, an implicit large-eddy-simulation approach, and domain decomposition in order to perform calculations on a parallel computing platform. Flow at a chord-based Reynolds number of 40,000 is considered in the investigation, which is characterized by laminar separation on the suction surface of the wing at low angles of attack. This separation then promotes transition to a more complex state, which can be modified by the use of plasma actuation. Several aspects of control are examined, including different actuator configurations, alternative plasma-force models, both continuous and pulsed modes of operation, and the magnitude of plasma force required for control.

Nomenclature

A	=	plasma-force pulsing amplitude function
c	=	airfoil chord
Cd	=	wing integrated drag coefficient
Cf	=	skin friction coefficient
Cl	=	wing integrated lift coefficient
Cm	=	wing integrated moment coefficient
Cp	=	surface pressure coefficient
D_c	=	plasma scale parameter
E	=	total specific energy
$\mathbf{E}$	=	nondimensional electric field vector
E_{k_z}, E_ω	=	nondimensional turbulent-kinetic-energy wave number and frequency spectral amplitudes
E_r	=	reference electric field magnitude
E_x, E_y, E_z	=	nondimensional components of the electric field vector
e_c	=	electron charge, 1.6×10^{-19} C
$\mathbf{F}, \mathbf{G}, \mathbf{H}$	=	inviscid vector fluxes
f	=	dimensional imposed actuator pulsing frequency
$\mathbf{F}_v, \mathbf{G}_v, \mathbf{H}_v$	=	viscous vector fluxes
k_z	=	nondimensional spanwise wave number
$\mathcal{J}$	=	Jacobian of the coordinate transformation
M	=	Mach number
p	=	nondimensional static pressure
Pr	=	Prandtl number, 0.73 for air
$\mathbf{Q}$	=	vector of dependent variables
$\mathcal{Q}_i$	=	components of the heat flux vector
q_c	=	nondimensional charge density
Re	=	reference Reynolds number, $\rho_\infty u_\infty c / \mu_\infty$
$\mathbf{S}$	=	source vector
T	=	nondimensional static temperature
t	=	nondimensional time
t_d	=	portion of fundamental period over which actuator is active
t_p	=	nondimensional actuator fundamental period
U, V, W	=	contravariant velocity components
u, v, w	=	nondimensional Cartesian velocity components in the x, y, and z directions
u_1, u_2, u_3	=	u, v, and w
x, y, z	=	nondimensional Cartesian coordinates in the streamwise, vertical, and spanwise directions
x_1, x_2, x_3	=	x, y, and z
α	=	angle of attack
γ	=	specific heat ratio, 1.4 for air
$\Delta \mathbf{Q}$	=	$\mathbf{Q}^{p+1} - \mathbf{Q}^p$
Δt	=	time-step size
δ_{ij}	=	Kronecker delta function
$\delta_{\xi 2}, \delta_{\eta 2}, \delta_{\zeta 2},$ $\delta_{\xi 6}, \delta_{\eta 6}, \delta_{\zeta 6}$	=	second-order and sixth-order finite difference operators in ξ, η, and ζ
μ	=	nondimensional molecular viscosity coefficient
ξ, η, ζ	=	nondimensional body-fitted computational coordinates
$\xi_t, \xi_x, \xi_y,$ $\xi_z, \eta_t, \eta_x,$ $\eta_y, \eta_z, \zeta_t,$ $\zeta_x, \zeta_y, \zeta_z$	=	metric coefficients of the coordinate transformation
ρ	=	nondimensional fluid density
ρ_c	=	electron charge number density, $1 \times 10^{11}/\text{cm}^3$
τ_{ij}	=	components of the viscous stress tensor
ω	=	nondimensional frequency
ω_a	=	nondimensional imposed actuator pulsing frequency, cf/u_∞

Subscripts

w	=	evaluated at the wing surface
∞	=	dimensional reference value

Superscripts

n	=	time level
p	=	subiteration level
$\hat{\ }$	=	filtered value

    *Senior Research Aerospace Engineer, Computational Sciences Branch, AFRL/RBAC. Associate Fellow AIAA.

    †Technical Area Leader, Computational Sciences Branch, AFRL/RBAC. Associate Fellow AIAA.

=   time-mean quantity

'   =   root-mean-square fluctuating quantity

I. Introduction

BECAUSE of their high maneuverability, unmanned micro air vehicles (MAVs) are currently being considered for performing a wide range of missions that cannot be carried out by more traditional configurations. Additional advantages of MAVs include low cost and human-factor effectiveness. Because of the small size and low speeds associated with the aforementioned applications, the representative Reynolds numbers involved are typically less than 60,000. At low to moderate angles of attack, the flow is characterized by a laminar regime over a significant portion of the airfoil, which is unable to sustain even a mild adverse pressure gradient. As a result, separation occurs, leading to a laminar bubble that breaks down to a more complex structure before reattachment. When the Reynolds number decreases for a fixed angle of attack, the laminar separation bubble grows in vertical extent, resulting in a substantial increase in drag and, as the angle of attack is increased (for a fixed Reynolds number), the separation bubble moves forward toward the leading edge and eventually bursts, thereby degrading airfoil performance. This situation occurs for both two-dimensional airfoils and three-dimensional wings of sufficient aspect ratios such that the flow is not dominated by tip effects.

Vehicle weight considerations in MAV design require the use of lightweight structures, thus making such configurations extremely sensitive to the location of the separation bubble and the transition process. This is particularly true in regard to maneuvering stability and response to gust loading, as well as to general aerodynamic performance. Active flow control offers the potential of reducing these deficiencies by modifying the location of separation and the process of transition.

The aerodynamics of low-Reynolds-number flows over wings and airfoils have been studied extensively for many years. Until recently, most of these studies have focused on the designs of model airplanes and glider configurations. While much of the literature describing these efforts is beyond the present investigation, there is a large body of more current work devoted specifically to the SD7003 airfoil [1–13], which is representative of the airfoils employed for MAVs and is the subject of the present simulations. The SD7003 airfoil geometric shape is shown in Fig. 1, and it has a maximum thickness-to-chord ratio of 0.085 and a maximum camber of 1.48%. Because of the low Reynolds number involved, most of the experiments carried out for this airfoil were conducted in water [1–5,9–11], although some wind-tunnel results are also reported [2,4]. Many of the measurements have been obtained via particle image velocimetry (PIV), providing time-mean velocity components and Reynolds stresses. Experiments performed for the same flow conditions (Reynolds number and angle of attack) in different facilities have found considerable variation in the locations of separation, transition, and reattachment [3,10]. This is indicative of the extreme sensitivity in low-Reynolds-number transitional flow experiments to levels of freestream turbulence intensity and its spectral content, resulting in a fairly unpredictable situation. In addition to rigid body measurements, experimental data have also been taken for pitching and plunging airfoils [4,9,11].

A considerable number of numerical simulations [2,4,6–9,11–13] have also been performed in order to gain insight into various aspects of the flow about the SD7003 airfoil. The majority of these computations have considered the two-dimensional Reynolds-averaged Navier–Stokes (RANS) equations, employing both turbulence and transition modeling to represent the flowfield [2,4,6,7,9,11]. The exceptions to this approach are the calculations of Galbraith and Visbal [8], Qin et al. [12], and Visbal et al. [13] who used large-eddy simulations (LESs) to directly capture the transitional process.

The use of plasma-based actuators has been found to be an effective means of actively controlling a variety of diverse flow situations. As an alternative to more complex mechanical or pneumatic systems, such devices have no moving parts, have low power requirements, have a fast time response, are surface adapting, can operate over a broad range of actuation frequencies, and require no plumbing or fluid supply. These considerations have spawned a number of experimental explorations that include rotorcraft blade control [14], lift enhancement for stationary and oscillating airfoils [15–17], plasma flaps and slats [18], dynamic stall [19], tip clearances in turbine blades [20], landing gear and bluff-body flows [21,22], turbine-blade flowfields [23–27], and aerodynamic control of unmanned air vehicles [28]. Several related numerical computations have also been performed, where modeling was typically used to represent plasma-induced body forces imparted by actuators on the fluid field. Such simulations have been carried out for the control of wall-bounded flows [29], wing sections [30], delta wings [31], low-pressure turbine blades [32,33], cylinder flowfields [34], and fully turbulent separations [35].

Dielectric-barrier-discharge (DBD) plasma actuators typically operate in the low radio frequency range (1–10 kHz), with voltage amplitudes of 5–10 kV. An overview of the design, optimization, and application of these actuators has been given by Corke and Post [25]. Experimental measurements indicate that time-averaged body forces generated by such DBD devices are the dominant mechanism for exerting control. Because of this, simple models that account for these forces may be effectively used in numerical calculations. This approach is particularly useful in the LES of complex transitional flows, which place severe demands upon computational resources.

The present investigation employs LES to explore the use of plasma-based actuation to control the subsonic flow past a SD7003 airfoil section at a chord-based Reynolds number of 40,000 and a 4.0 deg angle of attack. This work compliments the RANS computations of Jayaraman et al. [6], where a similar plasma model was employed, and higher angles of incidence were considered. At these higher angles before stall, the separation and transition locations move toward the leading edge, and the flow is dominated by a leading-edge vortex. For situations more representative of cruise conditions, the laminar bubble formation, transition, reattachment, and plasma-based control will be more accurately represented by LES. The aforementioned flow features can adversely affect both the lift and moment forces acting on the airfoil section, degrading stability characteristics and the response to gust loads. Plasma control offers the potential to mitigate these undesirable circumstances. In the sections to follow, the governing equations, empirical plasma model, numerical method, and LES approach are described. Details of the simulations are summarized, and numerical results are reported. Comparisons are made with available experimental data for the baseline flow where no control was enforced, and results of various control simulations are presented.

II. Governing Equations

The governing fluid equations are taken as the unsteady three-dimensional compressible unfiltered Navier–Stokes equations. Although these computations are considered to be LESs, it will be subsequently explained why, unlike more traditional approaches, the unfiltered equations are solved. After introducing a generalized time-dependent curvilinear coordinate transformation to a body-fitted system, the equations are cast in the following nondimensional conservative form:
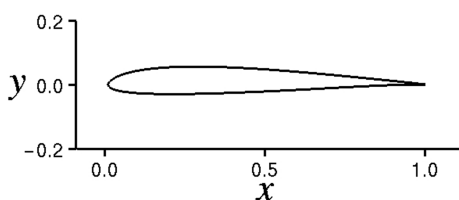

Fig. 1   SD7003 airfoil geometry.

$$\frac{\partial}{\partial t}\left(\frac{1}{\mathcal{J}}\boldsymbol{Q}\right) + \frac{\partial}{\partial \xi}\left(\boldsymbol{F} - \frac{1}{Re}\boldsymbol{F}_v\right) + \frac{\partial}{\partial \eta}\left(\boldsymbol{G} - \frac{1}{Re}\boldsymbol{G}_v\right)$$
$$+ \frac{\partial}{\partial \zeta}\left(\boldsymbol{H} - \frac{1}{Re}\boldsymbol{H}_v\right) = D_c q_c \boldsymbol{S} \tag{1}$$

Here t is the time, ξ, η, and ζ are the computational coordinates, $\boldsymbol{Q}$ is the vector of dependent variables, $\boldsymbol{F}$, $\boldsymbol{G}$, and $\boldsymbol{H}$ are the inviscid flux vectors, $\boldsymbol{F}_v$, $\boldsymbol{G}_v$, and $\boldsymbol{H}_v$ are the viscous flux vectors, and $\boldsymbol{S}$ is the source vector representing the effect of plasma-induced body forces. The vector of dependent variables is given as

$$\boldsymbol{Q} = [\rho \quad \rho u \quad \rho v \quad \rho w \quad \rho E]^T \tag{2}$$

the vector fluxes are given by

$$\boldsymbol{F} = \frac{1}{\mathcal{J}}\begin{bmatrix} \rho U \\ \rho u U + \xi_x p \\ \rho v U + \xi_y p \\ \rho w U + \xi_z p \\ \rho E U + \xi_{x_i} u_i p \end{bmatrix}, \qquad \boldsymbol{G} = \frac{1}{\mathcal{J}}\begin{bmatrix} \rho V \\ \rho u V + \eta_x p \\ \rho v V + \eta_y p \\ \rho w V + \eta_z p \\ \rho E V + \eta_{x_i} u_i p \end{bmatrix}$$

$$\boldsymbol{H} = \frac{1}{\mathcal{J}}\begin{bmatrix} \rho W \\ \rho u W + \zeta_x p \\ \rho v W + \zeta_y p \\ \rho w W + \zeta_z p \\ \rho E W + \zeta_{x_i} u_i p \end{bmatrix} \tag{3}$$

$$\boldsymbol{F}_v = \frac{1}{\mathcal{J}}\begin{bmatrix} 0 \\ \xi_{x_i}\tau_{i1} \\ \xi_{x_i}\tau_{i2} \\ \xi_{x_i}\tau_{i3} \\ \xi_{x_i}(u_j\tau_{ij} - \mathcal{Q}_i) \end{bmatrix}, \qquad \boldsymbol{G}_v = \frac{1}{\mathcal{J}}\begin{bmatrix} 0 \\ \eta_{x_i}\tau_{i1} \\ \eta_{x_i}\tau_{i2} \\ \eta_{x_i}\tau_{i3} \\ \eta_{x_i}(u_j\tau_{ij} - \mathcal{Q}_i) \end{bmatrix}$$

$$\boldsymbol{H}_v = \frac{1}{\mathcal{J}}\begin{bmatrix} 0 \\ \zeta_{x_i}\tau_{i1} \\ \zeta_{x_i}\tau_{i2} \\ \zeta_{x_i}\tau_{i3} \\ \zeta_{x_i}(u_j\tau_{ij} - \mathcal{Q}_i) \end{bmatrix} \tag{4}$$

with the source term

$$\boldsymbol{S} = \frac{1}{\mathcal{J}}\begin{bmatrix} 0 \\ E_x \\ E_y \\ E_z \\ u E_x + v E_y + w E_z \end{bmatrix} \tag{5}$$

and

$$D_c = \frac{\rho_c e_c E_r c}{\rho_\infty u_\infty^2} \tag{6}$$

where

$$U = \xi_t + \xi_{x_i} u_i, \qquad V = \eta_t + \eta_{x_i} u_i, \qquad W = \zeta_t + \zeta_{x_i} u_i \tag{7}$$

$$E = \frac{T}{\gamma(\gamma - 1)M_\infty^2} + \frac{1}{2}(u^2 + v^2 + w^2) \tag{8}$$

In the preceding expressions, u, v, and w are the Cartesian velocity components, ρ is the density, p is the pressure, and T is the temperature. All length scales have been nondimensionalized by the airfoil chord c, and dependent variables have been normalized by reference values, except for p, which has been nondimensionalized by $\rho_\infty u_\infty^2$. Components of the heat flux vector and stress tensor are expressed as

$$\mathcal{Q}_i = -\left[\frac{1}{(\gamma - 1)M_\infty^2}\right]\left(\frac{\mu}{Pr}\right)\frac{\partial \xi_j}{\partial x_i}\frac{\partial T}{\partial \xi_j} \tag{9}$$

$$\tau_{ij} = \mu\left(\frac{\partial \xi_k}{\partial x_j}\frac{\partial u_i}{\partial \xi_k} + \frac{\partial \xi_k}{\partial x_i}\frac{\partial u_j}{\partial \xi_k} - \frac{2}{3}\delta_{ij}\frac{\partial \xi_l}{\partial x_k}\frac{\partial u_k}{\partial \xi_l}\right) \tag{10}$$

The Sutherland law for the molecular viscosity coefficient μ and the perfect gas relationship

$$p = \frac{\rho T}{\gamma M_\infty^2} \tag{11}$$

were also employed, and the Stokes hypothesis for the bulk viscosity coefficient has been invoked.

III. Empirical Plasma Model

Many quantitative aspects of the fundamental processes governing plasma/fluid interactions remain unknown or computationally prohibitive, particularly for transitional and turbulent flows. These circumstances have given rise to the development of a wide spectrum of models with varying degrees of sophistication that may be employed for more practical simulations. Among the simplified methods focused specifically on discharge/fluid coupling is that of Roth [36] and Roth et al. [37], who associated the transfer of momentum from ions to neutral particles based upon the gradient of electric pressure. A more refined approach, suitable for coupling with fluid response, was an empirical model proposed by Shyy et al. [38], using separate estimates for the charge distribution and electric field. Known plasma physics parameters were linked to experimental data. This representation has been successfully employed for several previous simulations of plasma-controlled flows [29–34], and its basic formulation was also largely adopted in the present investigation.

A schematic representation of a typical single asymmetric DBD plasma actuator is depicted in Fig. 2. The actuator consists of two electrodes that are separated by a dielectric insulator and mounted on a body surface. An oscillating voltage, in the 1–10 kHz frequency range, is applied across electrodes, developing an electric field about the actuator. When the imposed voltage is sufficiently high, the dielectric produces a barrier discharge that weakly ionizes the surrounding gas. Momentum acquired by the resulting charged particles from the electric field is transferred to the primary neutral molecules by a combination of electrodynamic body forces and poorly understood complex collisional interactions. Because the bulk fluid cannot respond rapidly to the high-frequency alternating voltage, the dominant effect of actuation is to impose a time-mean electric field on the external flow. In the numerical simulation of control applications, the entire process may be modeled as a body force vector acting on the net fluid adjacent to the actuator, which produces a flow velocity.

The model for the geometric extent of the plasma field generated by such an actuator is indicated in Fig. 3. The triangular region defined by line segments OA, OB, and AB constitutes the plasma boundary. Outside of this region, the electric field is not considered strong enough to ionize the air [38]. The electric field has its maximum value at point O and varies linearly within OAB. The peak value of the electric field can be estimated from the applied voltage and the spacing between the electrodes. Along segment AB, the electric field diminishes to its threshold value, which was taken as 30 kV/cm [38]. The electric body force is equal to $q_c\boldsymbol{E}$ and provides coupling from the plasma to the fluid, resulting in the source vector $\boldsymbol{S}$, appearing in Eq. (1). Some uncertainty exists regarding the direction of the force vector, which was related to the ratio OA/OB in the original work of Shyy et al. [38]. Within the region OAB, the charge density q_c is taken to be constant. The plasma scale parameter D_c arises from nondimensionalization of the governing equations and represents the ratio of the electrical force of the plasma to the inertial force of the fluid.
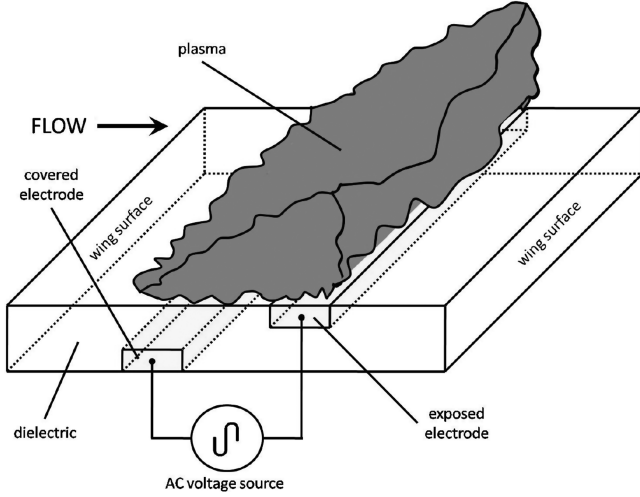
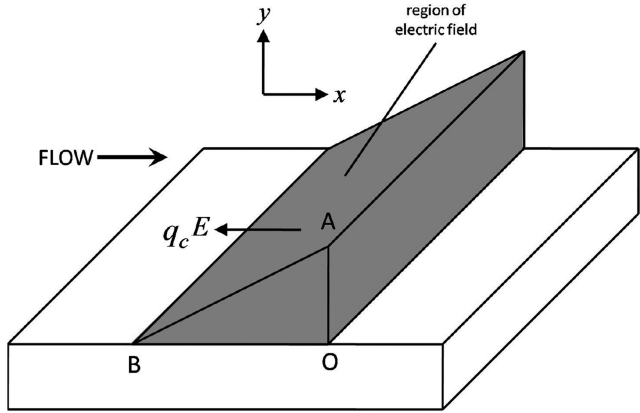Fig. 2   Schematic representation of plasma actuator.

Fig. 3   Geometry for the Shyy et al. [38] empirical plasma-force model.

Some specific details of the plasma model incorporated in the present simulations were specified corresponding to the original experiment of Shyy et al. [38]. The ratio of the threshold electric field magnitude to its peak value was set to 0.133, OA/OB was taken as 0.5, and OB = 0.025 (normalized by the airfoil chord). For the purposes of the present computations, it is assumed that actuator was mounted flush with the dielectric (wing) surface, and did not protrude above it, and that the direction of the force is tangential to the actuator surface. Because of empiricism of the formulation, there is ambiguity regarding the value of the scale parameter D_c, which could be varied during the investigation to produce more or less control. As indicated
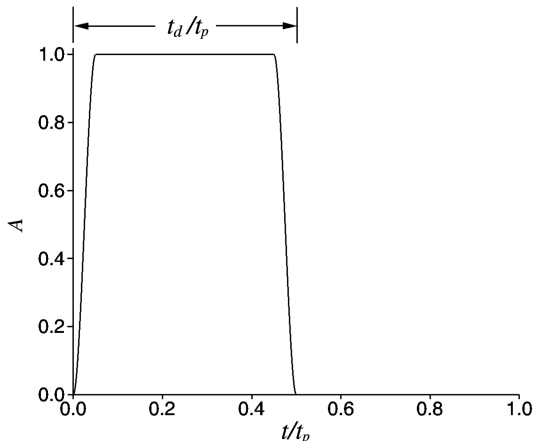

Fig. 4   Plasma actuator amplitude function time history.

in Figs. 2 and 3, the orientation of the actuators for all simulations reported here was such that the plasma body force opposed the primary flow direction (counterflow actuation).

DBD actuators are inherently unsteady devices. As mentioned previously, within the context of the empirical model, the body force imposed on the fluid is assumed to be steady owing to the high frequency of the applied voltage. In addition to a continuous mode of actuation, these devices may also be operated in a pulsed manner, as described by Corke and Post [25], thereby reducing total power consumption. The pulsed mode of operation also introduces low-frequency forcing to the flow, which may be more receptive to control and offers the potential of improved effectiveness. For simulation of pulsed actuation, the forcing amplitude is modulated according to a duty cycle, which is illustrated in Fig. 4. Here, t_d is the portion of the fundamental period t_p over which the device is active. The ratio $t_d/t_p \times 100$, expressed as a percentage, is commonly referred to as the duty cycle, which is 50% in the present case. The amplitude time history for one cycle appearing in the figure consists of a series of piecewise continuous cubic and linear functions that were used to represent the pulsing duration. The amplitude function was then appended as a factor to the plasma-force magnitude in order to establish pulsed control. This description is identical to that used by the authors in previous flow control simulations [32,35,39]. It should be noted that the applied waveform introduces multiple harmonics of the primary frequency, as was demonstrated in [29,40].

IV.   Numerical Method

Time-accurate solutions to Eq. (1) were obtained numerically by the implicit approximately-factored finite difference algorithm of Beam and Warming [41], employing Newton-like subiterations [42], which has evolved as an efficient tool for generating solutions to a wide variety of complex fluid flow problems and may be written as follows:

$$
\begin{aligned}
&\left[\frac{1}{\mathcal{J}} + \left(\frac{2\Delta t}{3}\right)\delta_{\xi 2}\left(\frac{\partial \boldsymbol{F}^p}{\partial \boldsymbol{Q}} - \frac{1}{Re}\frac{\partial \boldsymbol{F}_v^p}{\partial \boldsymbol{Q}}\right)\right]\mathcal{J} \times \left[\frac{1}{\mathcal{J}} + \left(\frac{2\Delta t}{3}\right)\delta_{\eta 2}\left(\frac{\partial \boldsymbol{G}^p}{\partial \boldsymbol{Q}}\right.\right.\\
&\left.\left. - \frac{1}{Re}\frac{\partial \boldsymbol{G}_v^p}{\partial \boldsymbol{Q}}\right)\right]\mathcal{J} \times \left[\frac{1}{\mathcal{J}} + \left(\frac{2\Delta t}{3}\right)\delta_{\zeta 2}\left(\frac{\partial \boldsymbol{H}^p}{\partial \boldsymbol{Q}} - \frac{1}{Re}\frac{\partial \boldsymbol{H}_v^p}{\partial \boldsymbol{Q}}\right)\right]\Delta\boldsymbol{Q}\\
&= -\left(\frac{2\Delta t}{3}\right)\left[\left(\frac{1}{2\Delta t}\right)\left(\frac{3\boldsymbol{Q}^p - 4\boldsymbol{Q}^n + \boldsymbol{Q}^{n-1}}{\mathcal{J}}\right)\right.\\
&+ \delta_{\xi 6}\left(\boldsymbol{F}^p - \frac{1}{Re}\boldsymbol{F}_v^p\right) + \delta_{\eta 6}\left(\boldsymbol{G}^p - \frac{1}{Re}\boldsymbol{G}_v^p\right)\\
&\left. + \delta_{\zeta 6}\left(\boldsymbol{H}^p - \frac{1}{Re}\boldsymbol{H}_v^p\right) - D_c q_c \boldsymbol{S}^p\right]
\end{aligned}
\tag{12}
$$

In this expression, which is employed to advance the solution in time, $\boldsymbol{Q}^{p+1}$ is the $p + 1$ approximation to $\boldsymbol{Q}$ at the $n + 1$ time level $\boldsymbol{Q}^{n+1}$, and $\Delta\boldsymbol{Q} = \boldsymbol{Q}^{p+1} - \boldsymbol{Q}^p$. For $p = 1$, $\boldsymbol{Q}^p = \boldsymbol{Q}^n$. Second-order-accurate backward-implicit time differencing was used to obtain temporal derivatives.

The implicit segment of the algorithm [left-hand side of Eq. (12)] incorporates second-order-accurate centered differencing for all spatial derivatives and uses nonlinear artificial dissipation [43] to augment stability. For simplicity, the dissipation terms are not shown in Eq. (12). Efficiency is enhanced by solving this implicit portion of the factorized equations in diagonalized form [44]. Temporal accuracy, which can be degraded by use of the diagonal form, is maintained by using subiterations within a time step. This technique has been commonly invoked in order to reduce errors due to factorization, linearization, diagonalization, and explicit application of boundary conditions. It is useful for achieving temporal accuracy on overset zonal mesh systems and for a domain decomposition implementation on parallel computing platforms. Any deterioration of the solution caused by use of artificial dissipation and by lower-order spatial resolution of implicit operators is also reduced by the procedure. Three subiterations per time step have been applied in the current simulations to preserve second-order temporal accuracy.

The compact difference scheme employed on the right-hand side of Eq. (12) is based upon the pentadiagonal system of Lele [45] and is capable of attaining spectral-like resolution. This is achieved through the use of a centered implicit difference operator with a compact stencil, thereby reducing the associated discretization error. For the present computations, a sixth-order tridiagonal subset of Lele's system is used, which is illustrated here in one spatial dimension as

$$\alpha_d \left(\frac{\partial \boldsymbol{F}}{\partial \xi} \right)_{i-1} + \left(\frac{\partial \boldsymbol{F}}{\partial \xi} \right)_i + \alpha_d \left(\frac{\partial \boldsymbol{F}}{\partial \xi} \right)_{i+1} = a \left(\frac{\boldsymbol{F}_{i+1} - \boldsymbol{F}_{i-1}}{2} \right)$$
$$+ b \left(\frac{\boldsymbol{F}_{i+2} - \boldsymbol{F}_{i-2}}{4} \right) \qquad (13)$$

with $\alpha_d = 1/3$, $a = 14/9$, and $b = 1/9$. The scheme has been adapted by Visbal and Gaitonde [46] as an implicit iterative time-marching technique, applicable for unsteady vortical flows, and has been used to obtain the spatial derivative of any scalar, flow variable, metric coefficient, or flux component. It is employed in conjunction with a low-pass Pade-type nondispersive spatial filter developed by Gaitonde et al. [47], which has been shown to be superior to the use of explicitly added artificial dissipation for maintaining both stability and accuracy on stretched curvilinear meshes [46]. The filter is applied to the solution vector sequentially in each of the three computational directions following each subiteration, and it is implemented in one dimension as

$$\alpha_f \hat{\boldsymbol{Q}}_{i-1} + \hat{\boldsymbol{Q}}_i + \alpha_f \hat{\boldsymbol{Q}}_{i+1} = \sum_{n=0}^{4} \frac{a_n}{2} (\boldsymbol{Q}_{i+n} + \boldsymbol{Q}_{i-n}) \qquad (14)$$

where $\hat{\boldsymbol{Q}}$ designates the filtered value of $\boldsymbol{Q}$. It is noted that the filtering operation is a postprocessing technique, applied to the evolving solution in order to regularize features that are captured but poorly resolved. Equation (14) represents a one-parameter family of eighth-order filters, where numerical values for the a_ns may be found in [48]. The filter coefficient α_f is a free adjustable parameter that may be selected for specific applications, and it has been set to 0.30 for the present simulations.

The aforementioned features of the numerical algorithm are embodied in a parallel version of the time-accurate three-dimensional computer code FDL3DI [48], which has proven to be reliable for steady and unsteady fluid flow problems, including vortex breakdown [49,50], transitional wall jets [51], synthetic jet actuators [52], roughness elements [53], plasma flows [29–34], and direct numerical and LESs of subsonic [54,55] and supersonic flowfields [56,57].

V.   Large-Eddy Simulation Approach

In the LES approach, physical dissipation at the Kolmogorov scale is not represented, thereby allowing for less spatial resolution and a savings in computational resources. For nondissipative numerical schemes, without use of subgrid-scale (SGS) models, this leads to an accumulation of energy at high mesh wave numbers and, ultimately, to numerical instability. Traditionally, explicitly added SGS models are then used as a means to dissipate this energy. In the present methodology, the effect of the smallest fluid structures is accounted for by an implicit LES (ILES) technique, which has been successfully employed for a number of turbulent and transitional computations. The present ILES approach was first introduced by Visbal and Rizzetta [58] and Visbal et al. [59] as a formal alternative to conventional methodologies, and it is predicated upon the high-order compact differencing and low-pass spatial filtering schemes, without the inclusion of additional SGS modeling. This technique is similar to monotonically integrated LES (MILES) [60] in that it relies upon the numerical solving procedure to provide the dissipation that is typically supplied by conventional SGS models. Unlike MILES, however, dissipation is contributed by the aforementioned high-order Pade-type low-pass filter only at high spatial wave numbers where the solution is poorly resolved. This provides a mechanism for the turbulence energy to be dissipated at scales that cannot be

accurately resolved on a given mesh system, in a fashion similar to subgrid modeling. For purely laminar flows, filtering may be required to maintain numerical stability and preclude a transfer of energy to high-frequency spatial modes due to spurious numerical events. The ILES methodology thereby permits a seamless transition from LES to direct numerical simulation as the resolution is increased. In the ILES approach, the unfiltered governing equations may be employed, and the computational expense of evaluating subgrid models, which can be substantial, is avoided. This procedure also enables the unified simulation of flowfields where laminar, transitional, and turbulent regions simultaneously coexist.

It should also be noted that the ILES technique may be interpreted as an approximate deconvolution SGS model [61], which is based upon a truncated series expansion of the inverse filter operator for the unfiltered flowfield equations. Mathew et al. [62] have shown that filtering provides a mathematically consistent approximation of unresolved terms arising from any type of nonlinearity. Filtering regularizes the solution and generates virtual subgrid model terms that are equivalent to those of approximate deconvolution.

VI.   Details of the Computations

A.   Computational Meshes

An O-grid topology about the airfoil was used to represent the grid-point distribution of the numerical flowfield. A planar section of the computational mesh at a fixed spanwise location appears in Fig. 5. Only a fraction of the total grid points are seen in the figure. The entire mesh consisted of $651 \times 395 \times 151$ points in the circumferential, surface-normal, and spanwise directions, respectively. Automated software [63] was used to generate the planar section, which had a minimum normal spacing at the wall of 5.0×10^{-5} and extended to an outer boundary that was located approximately 100 chord from the airfoil surface. The 651 circumferential grid lines included a five-point overlap at the leading edge, where periodic conditions were applied. Planar O grids were distributed uniformly across the span of the wing so that the z spacing was constant. The extent of the spanwise domain was set to 0.2, a distance shown to be optimal for the previous similar computation of Galbraith and Visbal [8]. Periodic conditions were also enforced in
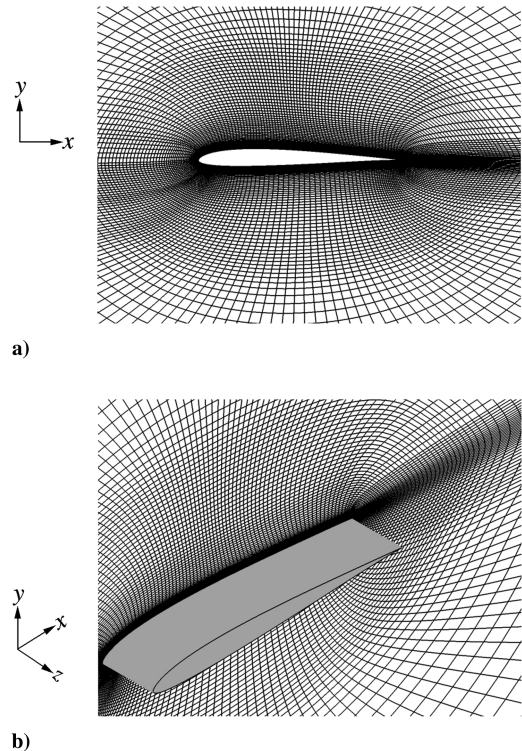
a)

b)

Fig. 5   Computational mesh for the SD7003 airfoil.

Table 1　Computational mesh parameters

Grid designation	Grid size
Fine	$(651 \times 395 \times 151)$
Medium	$(494 \times 297 \times 114)$
Coarse	$(396 \times 198 \times 76)$

the spanwise direction, again employing a five-point overlap for this purpose.

In addition to the aforementioned $651 \times 395 \times 151$-point grid, two auxiliary mesh systems were developed for the purpose of assessing the effect of spatial resolution on the resulting simulations. Each of these grids maintained the identical regions of clustering and mesh stretching ratios as those of the finer mesh distribution. Sizes for all three grids are given in Table 1.

B.　Boundary Conditions

On the wing surface, the no slip condition was enforced, along with an isothermal wall and a third-order-accurate implementation of a zero normal pressure gradient. Along the outer far-field boundary, freestream conditions were specified for all dependent variables. Grid stretching was employed in the far-field region to transfer information to high spatial wave numbers, and it was then dissipated

a)

b)

Fig. 6　Actuator configurations: a) standard actuator and b) serpentine actuator.

by the low-pass numerical filter [64]. This technique prevents any spurious reflections, particularly in the outflow area of the computational domain.

C.　Temporal Considerations

The time step for all calculations was prescribed as $\Delta t = 0.0001$. Once a baseline solution was obtained for the case without control, flowfields for all subsequent computations were initialized with that result. For coarser grids, interpolation was required. Solutions were then temporally evolved for 100,000 time steps in order to remove transients and attain and equilibrium state. Statistical information and time-mean values were then collected for an additional 100,000 steps, corresponding to 10 characteristic time units based upon the airfoil chord and freestream velocity. The nondimensional actuator pulsing frequency $\omega_a = 5.0$ was described by 2000 time steps per cycle. As will be shown later, this frequency was selected because it is representative of the shear-layer instability associated with the transitional flow over the wing.

D.　Actuator Configurations

Two different actuator configurations were considered in this investigation, which are exhibited in Fig. 6. Figure 6a is a standard configuration with no spanwise variation, corresponding to the geometry in Fig. 3. Figure 6b displays the novel serpentine actuator, which has been examined by Roy and Wang [65]. The purpose of the serpentine arrangement is to generate nonzero spanwise forces. The dark areas on the wing surfaces in the figures denote the regions between the exposed and covered electrodes and represent the footprint of the volumes containing the plasma force. There are no forces outside of these volumes.

E.　Plasma-Force Models

For the standard actuator configuration, the two-dimensional model of Shyy et al. [38] could be applied by distributing the force uniformly along the span of the wing. The model was also employed with the serpentine geometry by requiring the triangular region OAB of Fig. 3 to be perpendicular to the upstream and downstream extents of the actuator, shown in Fig. 6b. This specification also allows for a nonzero spanwise force. An alternative force model for the serpentine actuator has also been developed by Roy and Wang [65]. The distribution is a generalization of the model for a horseshoe-shaped configuration, which may be used for each of the semicircular portions of the serpentine arrangement. Unlike the Shyy et al. [38] model, which has its maximum force contribution at the exposed electrode (point O in Fig. 3), the corresponding maximum for the model of Roy and Wang [65] occurs at the midpoint between the electrodes. In addition, the model also has a nonzero wall-normal force component. A schematic representation of the force vectors for each of the models is found in Fig. 7.

As implemented in the simulations, force vectors were normalized by the maximum force magnitude for each model. The total force for each case was then determined by integrating the vectors over the volume of the forcefield. Because the plasma scale parameter D_c appears as a factor on the body force, its value was chosen in each
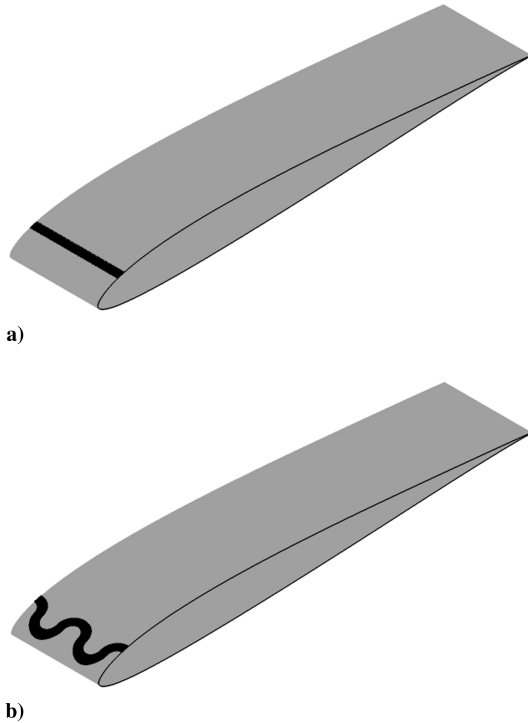

standard actuator
Shyy et al. [38] model

a)

serpentine actuator
Shyy et al. [38] model

b)

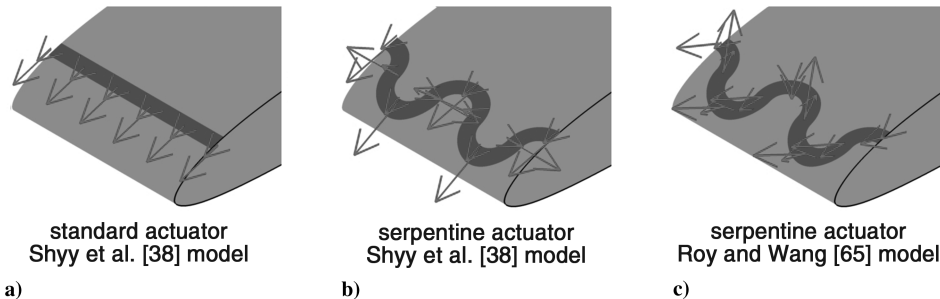serpentine actuator
Roy and Wang [65] model

c)

Fig. 7　Actuator force vectors: a) standard actuator/Shyy et al. [38] model, b) serpentine actuator/Shyy et al. [38] model, and c) serpentine actuator/Roy and Wang [65] model.

Table 2   Designation of cases

Case	Designation	Re	α	Grid	Actuator configuration	Force model	Mode of operation	D_c
1	Base	40,000	4.0	Fine	N/A	N/A	None	N/A
2	Base	41,700	3.5	Coarse	N/A	N/A	None	N/A
3	Base	41,700	3.5	Medium	N/A	N/A	None	N/A
4	Base	41,700	3.5	Fine	N/A	N/A	None	N/A
5	Std	40,000	4.0	Fine	Standard	Shyy et al. [38]	Continuous	39.27
6	Std	40,000	4.0	Fine	Standard	Shyy et al. [38]	Pulsed	39.27
7	Std	40,000	4.0	Fine	Standard	Shyy et al. [38]	Pulsed	9.82
8	Ser-S	40,000	4.0	Fine	Serpentine	Shyy et al. [38]	Continuous	25.00
9	Ser-S	40,000	4.0	Fine	Serpentine	Shyy et al. [38]	Pulsed	25.00
10	Ser-S	40,000	4.0	Fine	Serpentine	Shyy et al. [38]	Pulsed	6.25
11	Ser-R	40,000	4.0	Fine	Serpentine	Roy and Wang [65]	Continuous	161.62
12	Ser-R	40,000	4.0	Fine	Serpentine	Roy and Wang [65]	Pulsed	161.62
13	Ser-R	40,000	4.0	Fine	Serpentine	Roy and Wang [65]	Pulsed	40.41

Table 3   Time-mean results

Case	$\overline{Cl}$	$\overline{Cd}$	$\overline{Cm}$	$\overline{Cl/Cd}$
1	0.601	0.0276	−0.0433	21.7
2	0.576	0.0240	−0.0466	24.0
3	0.563	0.0250	−0.0467	22.5
4	0.563	0.0250	−0.0467	22.5
5	0.573	0.0228	−0.0294	25.2
6	0.560	0.0222	−0.0258	25.3
7	0.583	0.0225	−0.0309	25.9
8	0.553	0.0240	−0.0228	23.1
9	0.558	0.0227	−0.0250	24.6
10	0.559	0.0226	−0.0249	24.8
11	0.555	0.0233	−0.0235	23.8
12	0.561	0.0230	−0.0250	24.4
13	0.564	0.0221	−0.0256	25.5

4.0 deg. Baseline solutions on all mesh systems were also obtained for $Re = 41,700$ and $\alpha = 3.5$ deg, which match the experimental conditions of Katz [66], for which the results are available for comparison. In the control cases, $Re = 40,000$ and $\alpha = 4.0$ deg. A description of all cases is found in Table 2. Referring to the Table, some designations have been provided to more easily distinguish between various cases in the results to follow. The designation of Base will stand for baseline cases, Std will stand for the standard actuator with no spanwise variation, and Ser will stand for the serpentine configuration. The designations Ser-S and Ser-R will serve to differentiate between the serpentine actuator with the Shyy et al. [38] force model (Ser-S) and the serpentine actuator with the Roy and Wang [65] force model (Ser-R). As previously noted, cases 5, 8, 11, cases 6, 9, 12, and cases 7, 10, 13 have identical total integrated forces, respectively. Computed time-mean aerodynamic coefficients for all cases are given in Table 3.

case such that the total integrated forces were identical for the three situations seen in Fig. 7.

F. Description of Cases

All simulations were carried out at a freestream Mach number of $M_\infty = 0.1$. Computations of the baseline flow without control were performed at a Reynolds number of 40,000 and an angle of attack of

VII.   Baseline Case Without Control

This section describes results for cases with $Re = 41,700$ and $\alpha = 3.5$ deg. As noted earlier, these conditions correspond to those of an experiment for which measurements are available.
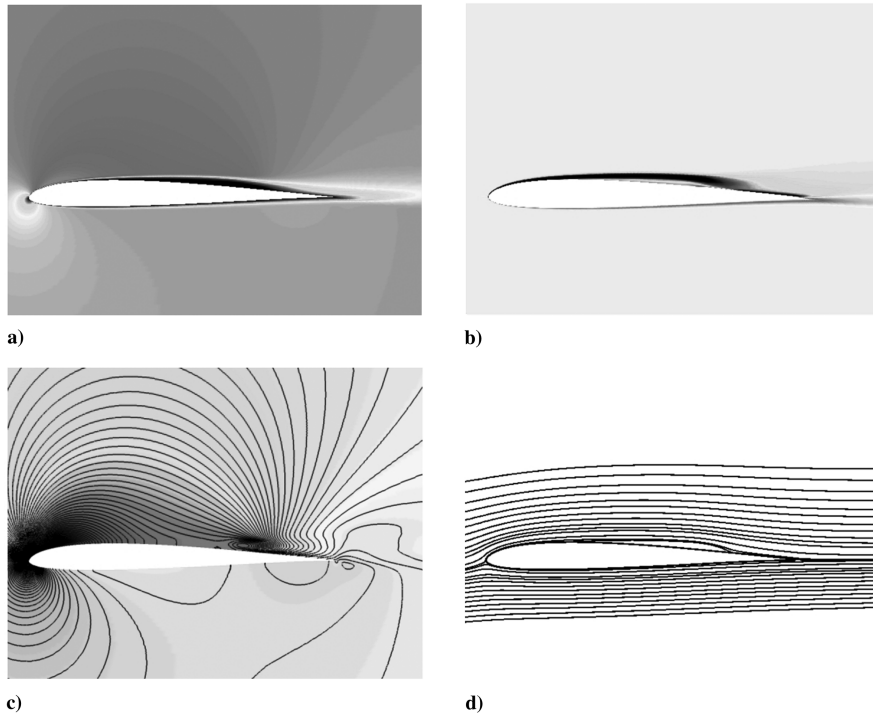

a)

b)

c)

d)

Fig. 8   Time-mean results for baseline case 4: a) u velocity contours, b) spanwise vorticity contours, c) Cp contours, and d) streamlines.
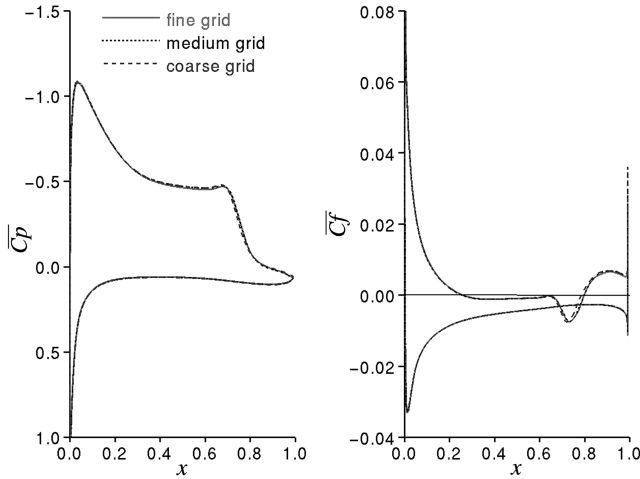
Fig. 9 Time-mean surface pressure and skin friction coefficient distributions for baseline cases 2–4.

A. Time-Mean Flowfields

Presented in Fig. 8 are time-mean planar contours of the streamwise velocity component u, the spanwise vorticity, pressure coefficient, and streamlines. In these and all other time-mean results to follow, variables have been averaged in the spanwise direction as well as temporally. The time-mean flow is characterized by a shallow separated region, which begins slightly downstream of $x = 0.2$. Reattachment occurs near $x = 0.8$. The zone of separated flow is apparent in the streamlines. Corresponding time-mean surface pressure and skin friction coefficient distributions are seen in Fig. 9. The plateau in pressure, where $\overline{Cp} = -0.5$, is representative of separation. Solutions on all three grid systems are shown in the figure, where little variation among them is observed.
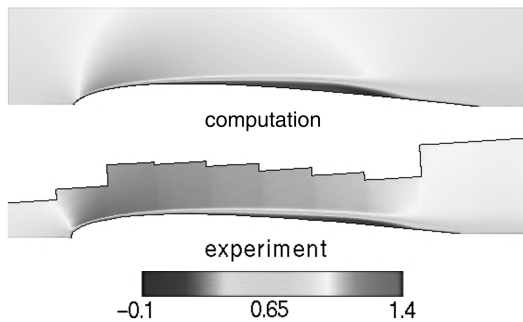
Fig. 10   Comparison of time-mean u velocity contours for baseline case 4.
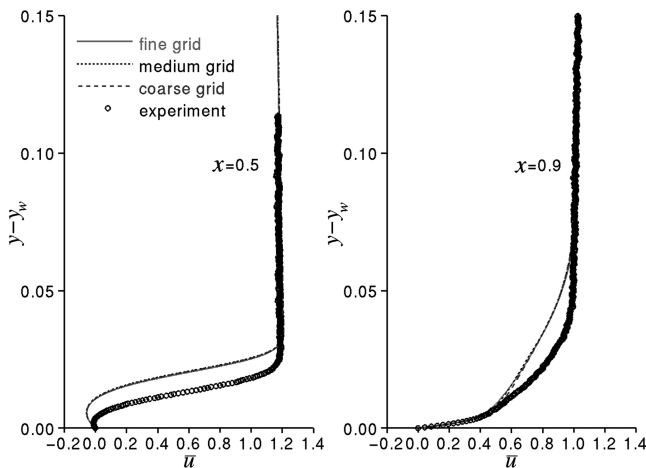
Fig. 11   Time-mean u velocity profiles for baseline cases 2–4.

PIV measurements were taken in water by Katz [66] at the specified flow conditions, and they are compared with the LES in Fig. 10. Contours of the u velocity component are displayed in the figure. It is apparent that the simulation has a somewhat larger extent of the separated flow region than that of the experiment. This is also demonstrated in time-mean profiles of the u velocity, appearing in Fig. 11. Profiles are indicated at the midchord location ($x = 0.5$) and in the trailing-edge region ($x = 0.9$). Because of the low Reynolds number, the disparity between the computation and the experiment is not necessarily surprising. It is noted that, for the even higher Reynolds number of $Re = 60,000$, the experimental investigation of Ol et al. [3], conducted in three different test facilities, produced widely varying results with regard to locations of separation, reattachment, and transition. A possible explanation for the differences seen in Figs. 10 and 11 is that some disturbance present in the experiment precipitated early transition to a more turbulent state, thereby mitigating the extent of separation.

Time-mean turbulent-kinetic-energy spanwise wave-number spectra are found in Fig. 12. These, and frequency spectra to be described later, were collected at a normal distance from the wing surface of $y - y_w \approx 0.005$. At the midchord location ($x = 0.5$), the energy is low because the flow is transitional. Closer to the trailing edge ($x = 0.9$), a more fully turbulent situation exists, and an inertial range is evident in the spectra. As expected, the finer grids can provide resolution to higher wave numbers.

B. Instantaneous Flowfields

Features of the instantaneous flowfield are illustrated in Fig. 13. Planar contours of the u velocity component and vorticity magnitude are given in Figs. 13a and 13b, respectively. Here it can be observed that a highly unsteady wake forms following transition. Figure 13c exhibits contours of the streamwise vorticity in the near-wall region. These contours reveal the transitional process that is occurring downstream of midchord. An isosurface of the Q criterion is represented in Fig. 13d . The Q criterion is defined as the difference between the vorticity magnitude and the rate-of-strain magnitude, and it is commonly used for vortex-core identification [67]. The Q criterion demonstrates that, following separation, the shear layer rolls up to form a series of coherent vortical structures. These eventually break down due to spanwise instabilities, forming a complex and chaotic situation in the trailing-edge region and downstream wake.

Figure 14 compares planar contours of the fluctuating velocity u' from the LES to the PIV of the experiment. Because the simulation produced a greater time-mean area of separation than that of the experiment, it also has a more pronounced region of large u'. This is also apparent in the u' profiles, shown in Fig. 15. Although the computed magnitudes of u' differ from those of the experiment, the shapes of the profiles are quite similar. It is also noted that only minor
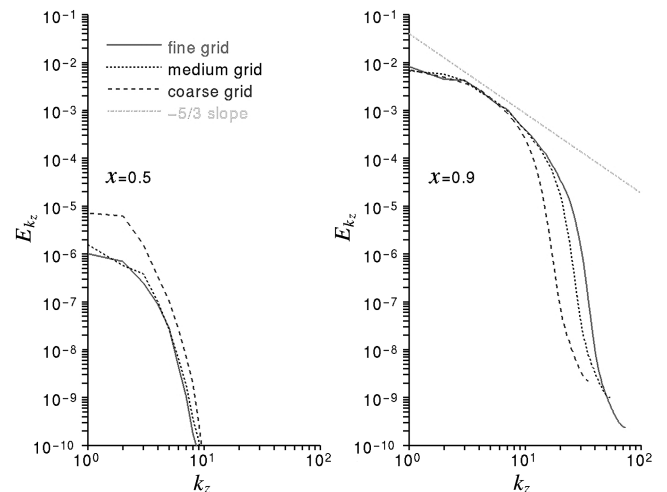

Fig. 12   Time-mean turbulent-kinetic-energy spanwise wave-number spectra for baseline cases 2–4.
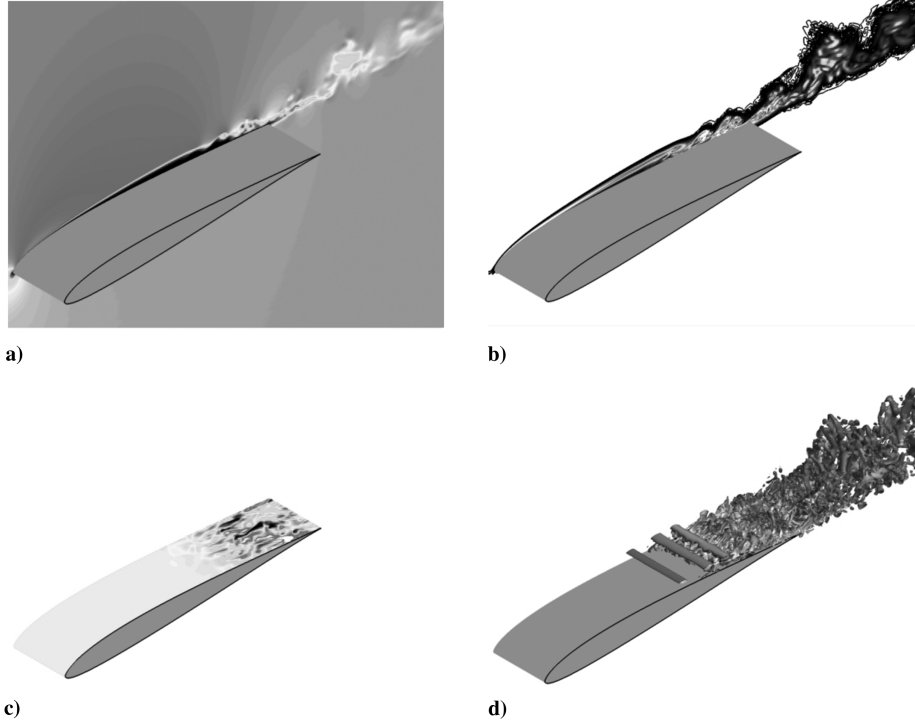
Fig. 13   Instantaneous results for baseline case 4: a) u **velocity contours, b) vorticity magnitude contours, c) contours of streamwise vorticity in the near-wall region, and d) isosurface of the** Q **criterion.**
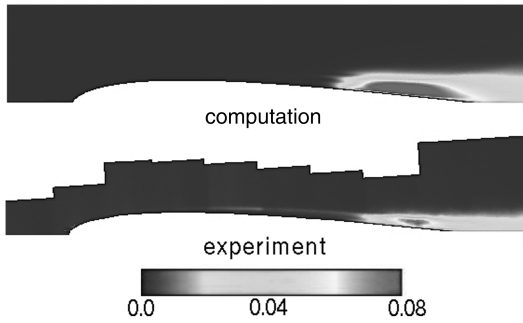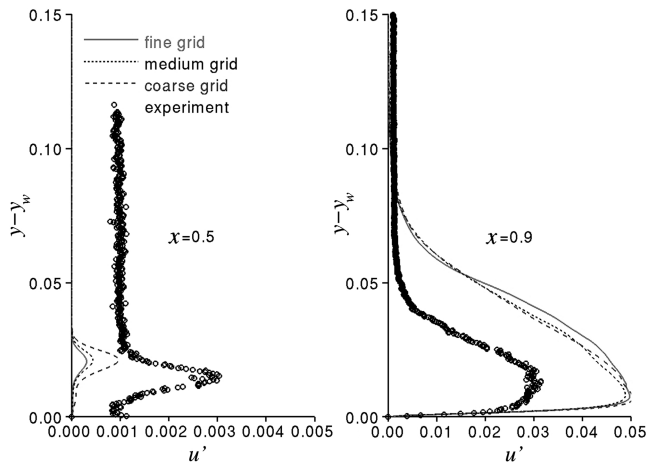

Fig. 14   Comparison of u' **contours for baseline case 4.**

Fig. 16   Spanwise-averaged turbulent-kinetic-energy frequency spectra for baseline case 4.

variations are indicated between solutions on respective grids, particularly those on the medium and fine meshes.

Displayed in Fig. 16 are spanwise-averaged turbulent-kinetic-energy frequency spectra. As in the wave-number spectra (Fig. 12), these also illustrate growth of turbulence in the trailing-edge region.
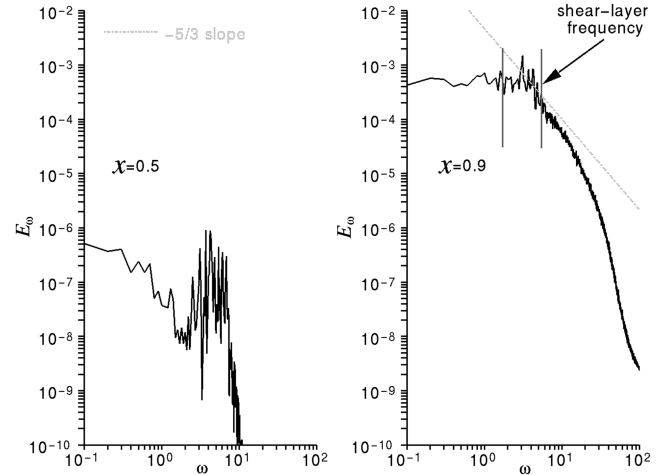
The portion of high amplitudes in the spectra, denoted in the figure, correspond to the inherent instability of the separating shear layer. The plasma actuator forcing frequency $\omega_a = 5.0$ is seen to fall in this range, and was selected to amplify the natural shear-layer instability and expedite the transitional process.

VIII.   Control Cases

All of the results reported in this section, including the baseline case without control, were obtained for $Re = 40,000$ and $\alpha = 4.0$ deg. Because of the number of cases considered in the investigation, features of the flowfields will focus primarily on cases 1, 6, 9, and 12, which are considered to be representative of the flows. This selection constitutes the baseline flow, the control cases for both actuator configurations, and both force models for the serpentine arrangement. Pulsed operation of the actuator is employed for these control cases, and the values of D_C represent the largest ones specified.

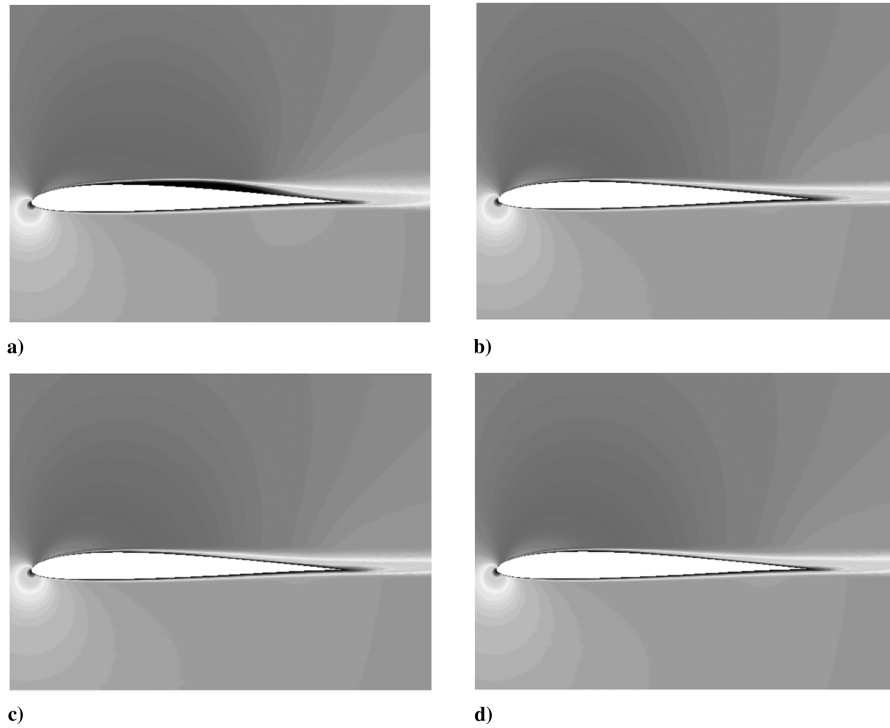**Fig. 15   Profiles of** u' **for baseline cases 2–4.**

Fig. 17 Time-mean planar contours of u velocity for baseline and control cases with pulsed actuation: a) case 1, Base; b) case 6, Std; c) case 9, Ser-S; and d) case 12, Ser-R.

A. Time-Mean Flowfields

Found in Fig. 17 are time-mean planar contours of the u velocity component for the four cases. It is evident that plasma control has reduced the extent of the boundary layer by precluding separation in the time-mean flowfield. This can also be seen in the streamlines of Fig. 18, where the flow has been fully attached in all the control cases. Corresponding surface pressure and skin friction coefficient distributions appear in Fig. 19. Because plasma actuation has eliminated separation ($\overline{Cf} > 0$), the pressure plateau is no longer present when control is enforced. This results in a loss of lift, but it is accompanied by a more appreciable loss in drag, such that the lift-to-drag ratio increases (see Table 3).

Figure 20 presents surface pressure and skin friction results for control cases employing continuous actuation. The values of D_c for these solutions are identical to those shown in Fig. 19. It is observed in the figure that separation is still present to an extent. The serpentine actuators are somewhat more effective, having eliminated most of the pressure plateau. Upon comparing Figs. 19 and 20, it can be concluded that continuous actuation is less effective than pulsed control. This conclusion was also made for plasma control of a low-pressure turbine blade [32].

The preceding conclusion is significant, because pulsed operation of the actuator lowers the power required for operation yet works more effectively. The magnitude of the plasma scale parameter D_c also directly relates to power requirements. Because of this, lower values of D_c were considered in the investigation. Provided in Fig. 21 are the surface pressure and skin friction distributions for pulsed operation when the values of D_c were reduced by a factor of 4.0. These results are quite similar to those of the higher D_c values in Fig. 19. This shows that pulsed operation of plasma actuators can be effective at low values of the total integrated forces and, correspondingly, low values of the required power.

Time-mean u velocity profiles for the control cases are given in Fig. 22. At the midchord station ($x = 0.5$), all the separated flow has been removed by plasma actuation, and near the trailing edge ($x = 0.9$), the control profiles have reached a more fully turbulent state.

B. Instantaneous Flowfields

Presented in Fig. 23 are time histories of the lift, drag, and moment coefficients (moment taken about $x = 0.25$). For each of these
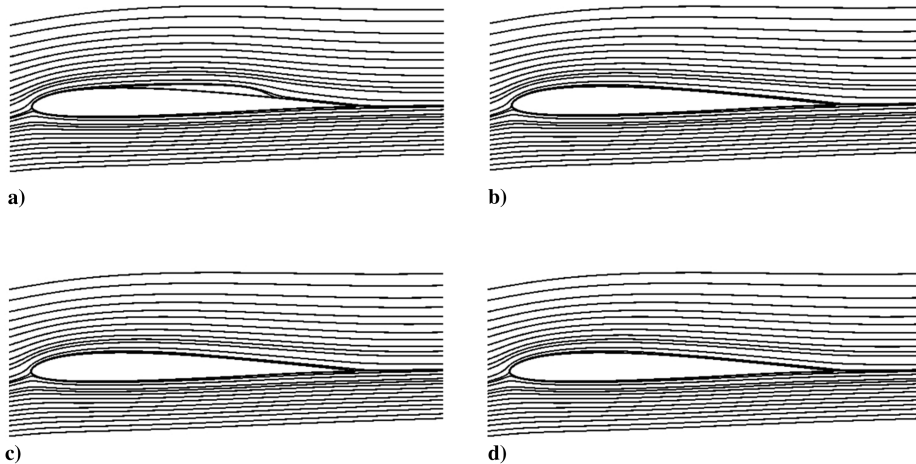

Fig. 18 Time-mean streamlines for baseline and control cases with pulsed actuation: a) case 1, Base; b) case 6, Std; c) case 9, Ser-S; and d) case 12, Ser-R.
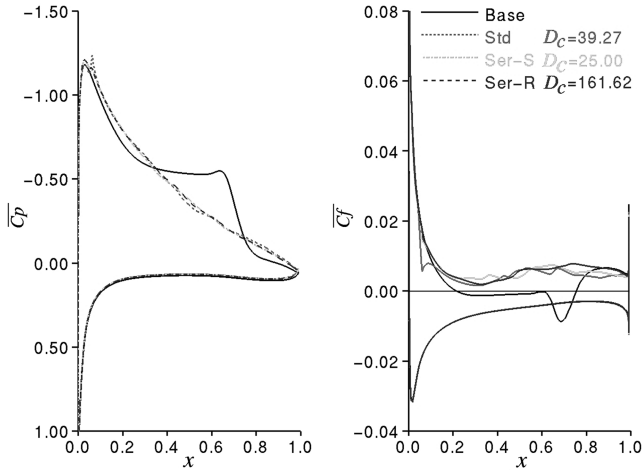
Fig. 19 Time-mean surface pressure and skin friction coefficient distributions for baseline (case 1) and control cases with pulsed actuation (cases 6, 9, and 12).
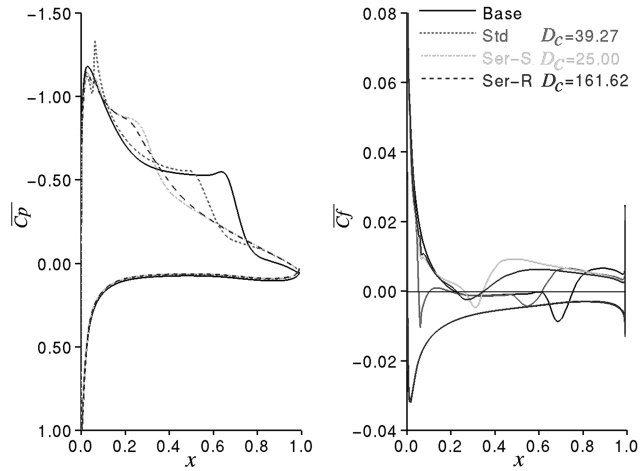

Fig. 20 Time-mean surface pressure and skin friction coefficient distributions for baseline (case 1) and control cases with continuous actuation (cases 5, 8, and 11).

coefficients, the large excursions exhibited in the figure are from the baseline simulation (case 1) and are due to the transitional, separated, and highly unstable nature of the boundary layer at a low Reynolds number. All of the control histories (cases 6, 9, 12) are grouped
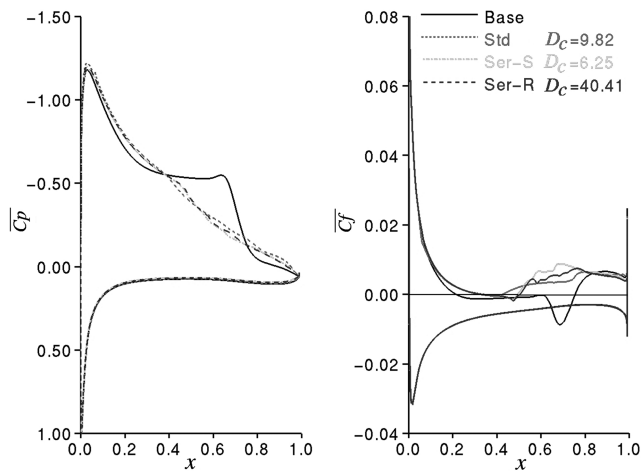

Fig. 21 Time-mean surface pressure and skin friction coefficient distributions for baseline (case 1) and control cases with pulsed actuation using minimum force contributions (cases 7, 10, and 13).
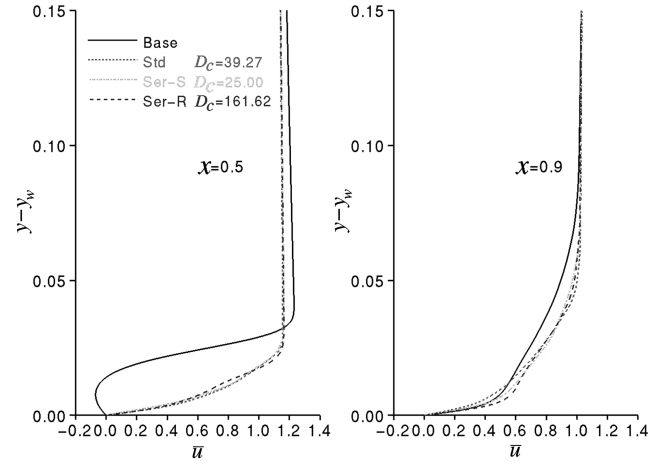

Fig. 22 Time-mean u velocity profiles for baseline (case 1) and control cases with pulsed actuation (cases 6, 9, and 12).

closely together, and there is little dependence upon either the actuator configuration or plasma-force model. As was noted earlier, the effect of control is to lower both the lift and drag while increasing the lift-to-drag ratio. The most significant percentage change relative to the baseline case, however, occurs in the moment coefficient. Because of this, it is thought that plasma-based control may be employed to improve stability and handling characteristics of MAVs, as well as for gust alleviation. In this regard, elimination of high-amplitude fluctuations in the aerodynamic coefficients for the baseline case is beneficial.

Figure 24 displays instantaneous planar contours of vorticity magnitude for the baseline and control cases. It is noted in the figure that the long laminar separated region before transition, which occurs in the baseline case, is absent for the control situations. When plasma actuation is employed, transition takes place further upstream, thereby precluding the formation of large vortical structures that convect downstream. This results in a decrease of the vertical extent of the wake when control is employed.

Isosurfaces of the Q criterion are seen in Fig. 25, which illustrate the physical mechanisms by which control is achieved. For this purpose, the pulsed actuation solutions in Figs. 25b–25d may be compared with the baseline flow of Fig. 25a. In the baseline isosurface, the coherent vortices generated by the laminar separated shear layer begin to break up at $x \approx 0.7$. When the standard actuator configuration is pulsed (Fig. 25b, case 6, Std), it creates a series of small coherent spanwise vortices that convect downstream and precipitate transition upstream of midchord. These vortices prevent
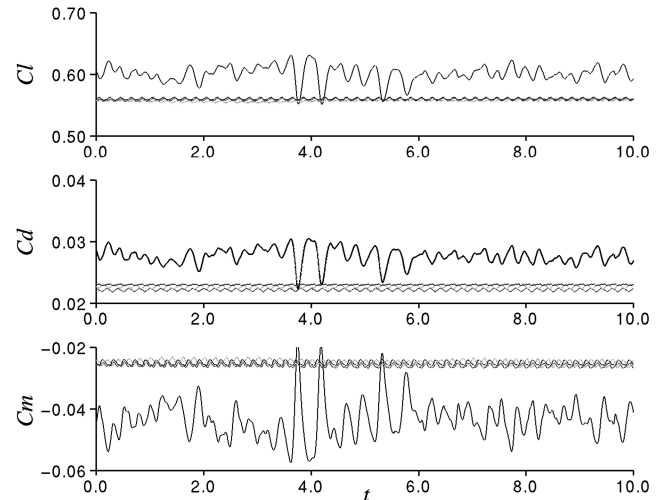

Fig. 23 Time histories of lift, drag, and moment coefficients for baseline (case 1) and control cases with pulsed actuation (cases 6, 9, and 12).
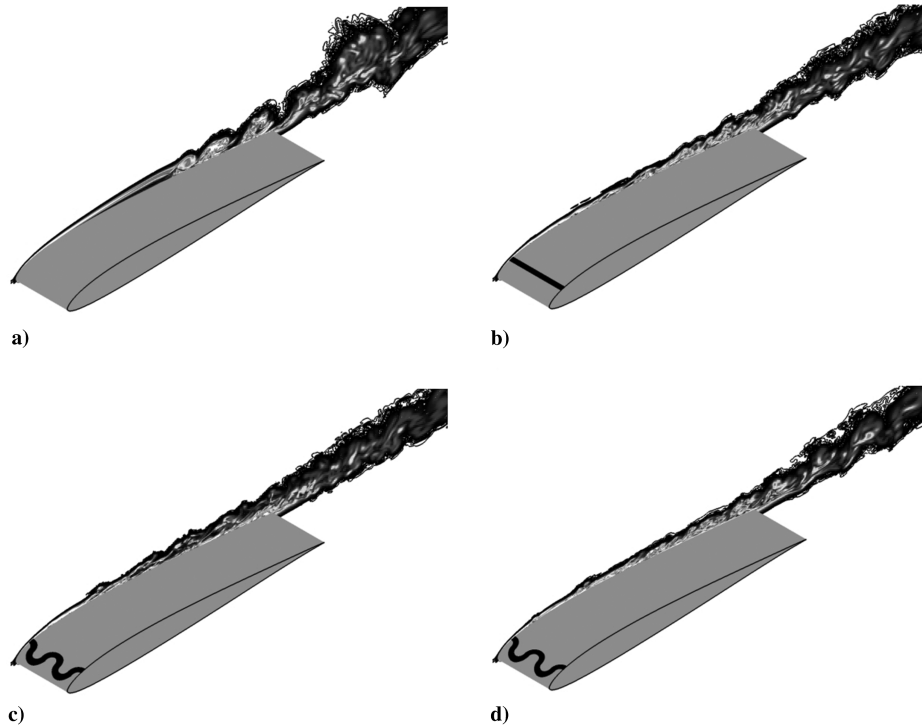
Fig. 24 Instantaneous planar contours of vorticity magnitude for baseline and control cases with pulsed actuation: a) case 1, Base; b) case 6, Std; c) case 9, Ser-S; and d) case 12, Ser-R.

laminar separation by bringing higher momentum fluid from the outer portion of the boundary layer toward the surface while, at the same time, removing lower momentum fluid from near the near-surface region. Thus, as transition occurs, the time-mean flow has always remained attached. Because of the nonuniform plasma-force distribution for the serpentine actuator (Figs. 25c and 25d), no coherent vortical structures are formed, but a rapid breakdown of the flow and transition to turbulence occurs just downstream of the

actuator location. In this situation, there appears to be little dependence upon the force model employed.

Found in Fig. 26 are profiles of the u' fluctuating velocity component. At the midchord location ($x = 0.5$), the magnitude of u' for the control cases is higher than that of the baseline because of the pulsed energy that has been added to the flow. In the trailing-edge region ($x = 0.9$), however, the baseline flow has developed large energy-containing structures. Since all the control cases prevented
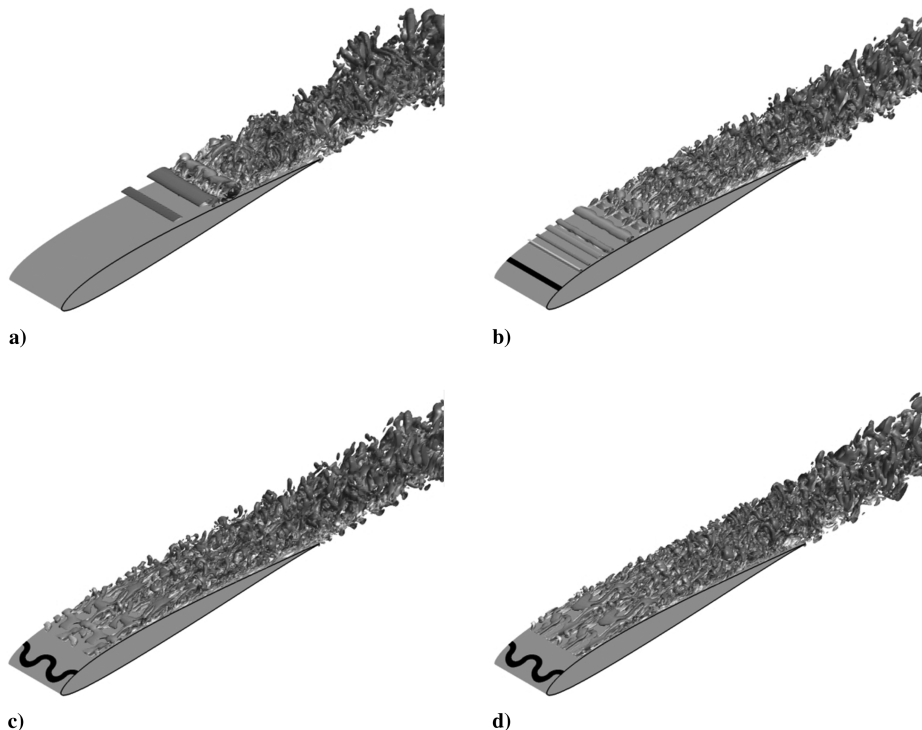

Fig. 25 Instantaneous isosurfaces of the Q criterion for baseline and control cases with pulsed actuation: a) case 1, Base; b) case 6, Std; c) case 9, Ser-S; and d) case 12, Ser-R.
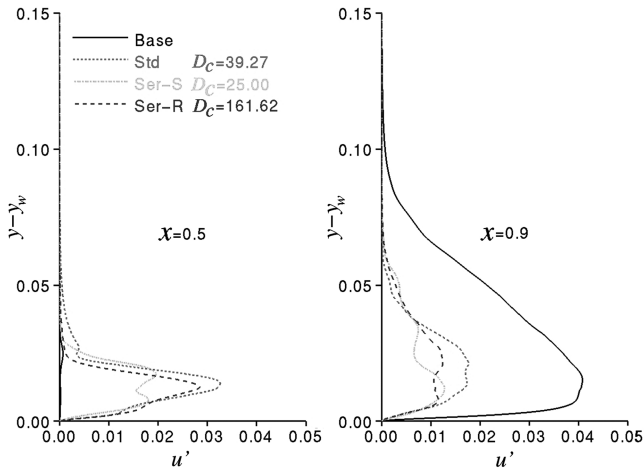
Fig. 26   Profiles of u' for baseline (case 1) and control cases with pulsed actuation (cases 6, 9, and 12).
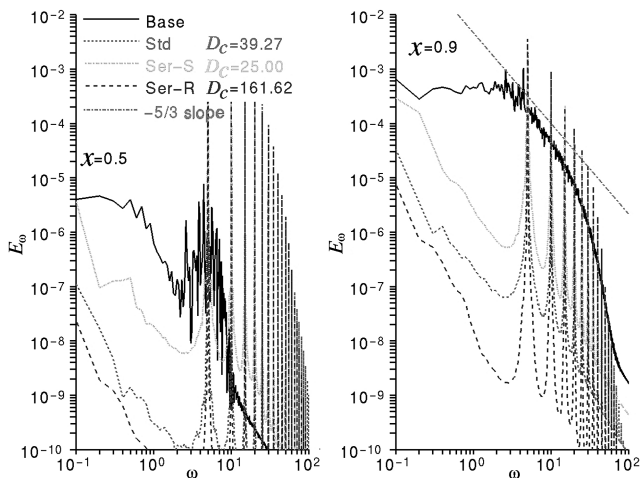

Fig. 27   Spanwise-averaged turbulent-kinetic-energy frequency spectra for baseline (case 1) and control cases with pulsed actuation (cases 6, 9, and 12).

development of these structures, u' is smaller than the baseline case at $x = 0.9$.

Turbulent-kinetic-energy frequency spectra appear in Fig. 27. Unlike the result indicated in Fig. 26, the energy of the baseline case at $x = 0.5$ is higher than that of the control solutions. The reasons for this are that the spectra were collected very near to the wing surface ($y - y_w \approx 0.005$), which is not clearly visible in Fig. 26, and that the turbulent energy is composed of other components in addition to u'. At $x = 0.9$, control cases contain less energy than the baseline, due to a lack of large-scale structures. Harmonics of the pulsing frequency are obvious in the control spectra. It is noted that the fundamental frequency lies in the unstable range of the baseline case, as it was selected to be.

IX.   Conclusions

LESs were carried out in order to explore the use of plasma-based control for flow over a finite span wing at a low Reynolds number, which is representative of MAV operations. A high-order numerical method was employed to simulate both conventional and serpentine actuator configurations, where simple phenomenological models provided body forces generated by the electric field of the plasma. A grid sensitivity study indicated that the spatial resolution was sufficient to accurately capture physical details of the computed flowfields. Both continuous and pulsed operations of the actuator were simulated, and alternate force models for the serpentine arrangement were considered. Actuators were positioned near the

wing leading edge, and pulsing was applied at the frequency associated with the unstable shear layer in order to facilitate transition. The magnitude of the applied body force was varied in order to determine the most efficient control situation.

It was found that the pulsed mode of operation was far superior to that of continuous actuation. Although the continuous mode was able to achieve some control, pulsing attained better performance and decreased power requirements. This result had also been seen in previous plasma actuator applications. When magnitudes of the plasma forces were decreased, efficiency increased. This is because the drag associated with the counterflow actuation was reduced. Lower force magnitudes were still able to expedite transition, which is the fundamental basis for the control.

Both the standard and serpentine actuators performed equally well, although the physical mechanisms governing the control were different for each. With the standard actuator, a series of small coherent spanwise vortices were generated by the pulsing and maintained time-mean attached flow before transition. For the serpentine configuration, the nonuniform spanwise force distribution suppressed the appearance of coherent two-dimensional modes and rapidly accelerated transition. There appeared to be little dependence on the specific details of the plasma-force model for the serpentine cases.

It should be noted that control strategies other than the ones considered here may be equally useful. In the present study, only counterflow plasma control has been investigated, where the actuator was positioned near the wing leading edge. Other locations are certainly possible. Previous works have demonstrated, for other applications, that coflow control that creates a wall jet near a solid boundary can also be used, and it has been shown in some cases that duty cycles as low as 10% can afford as much control effectiveness as those of higher values.

References

[1] Hanff, E. S., "PIV Application in Advanced Low Reynolds Number Facility," *IEEE Transactions on Aerospace and Electronic Systems*, Vol. 40, No. 1, Jan. 2004, pp. 310–319.
doi:10.1109/TAES.2004.1292162

[2] Yuan, W., Khalid, M., Windte, J., Scholz, U., and Radespiel, R., "An Investigation of Low-Reynolds-Number Flows Past Airfoils," AIAA Paper 2005-4607, June 2005.

[3] Ol, M. V., McAuliffe, B. R., Hanff, E. S., Scholz, U., and Kahler, C., "Comparison of Laminar Separation Bubble Measurements on a Low Reynolds Number Airfoil in Three Facilities," AIAA Paper 2005-5149, June 2005.

[4] Radespiel, R., Windte, J., and Scholz, U., "Numerical and Experimental Flow Analysis of Moving Airfoils with Laminar Separation Bubbles," AIAA Paper 2006-501, Jan. 2006.

[5] Brugmann, S., Brucker, C., and Schroder, W., "Scanning PIV Measurements of a Laminar Separation Bubble," *Experiments in Fluids*, Vol. 41, No. 2, Aug. 2006, pp. 319–326.
doi:10.1007/s00348-006-0153-6

[6] Jayaraman, B., Lian, Y., and Shyy, W., "Low-Reynolds Number Flow Control Using Dielectric Barrier Discharge Actuators," AIAA Paper 2007-3974, June 2007.

[7] Lian, Y., and Shyy, W., "Laminar-Turbulent Transition of a Low Reynolds Number Rigid or Flexible Airfoil," *AIAA Journal*, Vol. 45, No. 7, July 2007, pp. 1501–1513.
doi:10.2514/1.25812

[8] Galbraith, M. C., and Visbal, M. R., "Implicit Large Eddy Simulation of Low Reynolds Number Flow Past the SD7003 Airfoil," AIAA Paper 2008-0225, Jan. 2008.

[9] Lian, Y., Ol, M. V., and Shyy, W., "Comparative Study of Pitch-Plunge Airfoil Aerodynamics at Transitional Reynolds Number," AIAA

Paper 2008-0652, Jan. 2008.

[10] Brugmann, S., and Schroder, W., "Investigation of the Vortex Induced Unsteadiness of a Separation Bubble via Time-Resolved Scanning PIV Measurements," *Experiments in Fluids*, Vol. 45, No. 4, Oct, 2008, pp. 675–691.
doi:10.1007/s00348-008-0548-7

[11] Kang, C.-K., Baik, Y. S., Bernal, L., Ol, M. V., and Shyy, W., "Fluid Dynamics of Pitching and Plunging Airfoils of Reynolds Number 1×10^4 and 6×10^4," AIAA Paper 2009-536, Jan. 2009.

[12] Qin, S., Zhuang, M., Visbal, M. R., Galbraith, M. C., Lian, Y., and Shyy, W., "Local and Global Stability Analysis on Flows Around a SD7003 Airfoil," AIAA Paper 2009-1470, Jan. 2009.

[13] Visbal, M. R., Gordnier, R. E., and Galbraith, M. C., "High-Fidelity Simulations of Moving and Flexible Airfoils at Low Reynolds Numbers," *Experiments in Fluids*, Vol. 46, No. 5, May 2009, pp. 903–922.
doi:10.1007/s00348-009-0635-4

[14] Lorber, P., McCormick, D., Anderson, T., Wake, D., MacMartin, D., Pollack, M., Corke, T., and Breuer, K., "Rotorcraft Retreating Blade Stall Control," AIAA Paper 2000-2475, June 2000.

[15] Corke, T. C., Jumper, E. J., Post, M. L., Orlov, D., and McLaughlin, T. E., "Application of Weakly-Ionized Plasmas as Wing Flow-Control Devices," AIAA Paper 2002-0350, Jan. 2002.

[16] Post, M. L., and Corke, T. C., "Separation Control on High Angle of Attack Airfoil Using Plasma Actuators," *AIAA Journal*, Vol. 42, No. 11, Nov. 2004, pp. 2177–2184.
doi:10.2514/1.2929

[17] Post, M. L., and Corke, T. C., "Separation Control Using Plasma Actuators: Stationary and Oscillating Airfoils," AIAA Paper 2004-0841, Jan. 2004.

[18] Corke, T. C., He, C., and Patel, M. P., "Plasma Flaps and Slats: An Application of Weakly-Ionized Plasma Actuators," AIAA Paper 2004-2127, June–July 2004.

[19] Post, M. L., and Corke, T. C., "Separation Control Using Plasma Actuators: Dynamic Stall Vortexc Control on Oscillating Airfoil," *AIAA Journal*, Vol. 44, No. 12, Dec. 2006, pp. 3125–3135.
doi:10.2514/1.22716

[20] Morris, S. C., Corke, T. C., VanNess, D., Stephens, J., and Douville, T., "Tip Clearance Control Using Plasma Actuators," AIAA Paper 2005-0782, Jan. 2005.

[21] Thomas, F. O., Kozlov, A., and Corke, T. C., "Plasma Actuators for Landing Gear Noise Reduction," AIAA Paper 2005-3010, May 2005.

[22] Thomas, F. O., Kozlov, A., and Corke, T. C., "Plasma Actuators for Bluff Body Flow Control," AIAA Paper 2006-2845, June 2006.

[23] List, J., Byerley, A. R., McLaughlin, T. E., and Dyken, R. D., "Using a Plasma Actuator to Control Laminar Separation on a Linear Cascade Turbine Blade," AIAA Paper 2003-1026, Jan. 2003.

[24] Huang, J., Corke, T. C., and Thomas, F. O., "Plasma Actuators for Separation Control of Low Pressure Turbine Blades," AIAA Paper 2003-1027, Jan. 2003.

[25] Corke, T. C., and Post, M. L., "Overview of Plasma Flow Control: Concepts, Optimization, and Applications," AIAA Paper 2005-0563, Jan. 2005.

[26] Huang, J., Corke, T. C., and Thomas, F. O., "Plasma Actuators for Separation Control of Low-Pressure Turbine Blades," *AIAA Journal*, Vol. 44, No. 1, Jan. 2006, pp. 51–57.
doi:10.2514/1.2903

[27] Huang, J., Corke, T. C., and Thomas, F. O., "Unsteady Plasma Actuators for Separation Control of Low-Pressure Turbine Blades," *AIAA Journal*, Vol. 44, No. 7, July 2006, pp. 1477–1487.
doi:10.2514/1.19243

[28] Patel, M. P., Ng, T. T., Vasudevan, S., Corke, T. C., and He, C., "Plasma Actuators for Hingeless Aerodynamic Control of an Unmanned Air Vehicle," AIAA Paper 2006-3495, June 2006.

[29] Visbal, M. R., Gaitonde, D. V., and Roy, S., "Control of Transitional and Turbulent Flows Using Plasma-Based Actuators," AIAA Paper 2006-3230, June 2006.

[30] Gaitonde, D. V., Visbal, M. R., and Roy, S., "Control of Flow Past a Wing Section with Plasma-Based Body Forces," AIAA Paper 2005-5302, June 2005.

[31] Visbal, M. R., and Gaitonde, D. V., "Control of Vortical Flows Using Simulated Plasma Actuators," AIAA Paper 2006-0505, Jan. 2005.

[32] Rizzetta, D. P., and Visbal, M. R., "Numerical Investigation of Plasma-Based Flow Control for Transitional Highly Loaded Low-Pressure Turbine," *AIAA Journal*, Vol. 45, No. 10, Oct. 2007, pp. 2554–2564.
doi:10.2514/1.29602

[33] Rizzetta, D. P., and Visbal, M. R., "Plasma-Based Flow Control Strategies for Transitional Highly Loaded Low-Pressure Turbines," *Journal of Fluids Engineering*, Vol. 130, No. 4, April 2008,

Paper 041104.
doi:10.1115/1.2903816

[34] Rizzetta, D. P., and Visbal, M. R., "Large Eddy Simulation of Plasma-Based Control Strategies for Bluff Body Flow," *AIAA Journal*, Vol. 47, No. 3, March 2009, pp. 717–729.
doi:10.2514/1.39168

[35] Rizzetta, D. P., and Visbal, M. R., "Large-Eddy Simulation of Plasma-Based Turbulent Boundary- Layer Separation Control," AIAA Paper 2009-4287, June 2009.

[36] Roth, J. R., "Aerodynamic Flow Acceleration Using Paraelectric and Peristaltic Electrohydrodynamic Effects of a One Atmosphere Uniform Glow Discharge Plasma," *Physics of Plasmas*, Vol. 10, No. 5, May 2003, pp. 2117–2128.
doi:10.1063/1.1564823

[37] Roth, J. R., Sin, H., and Madham, R. C. M., "Flow Re-Attachment and Acceleration by Paraelectric and Peristaltic Electrohydrodynamic (EHD) Effects," AIAA Paper 2003-0531, Jan. 2003.

[38] Shyy, W., Jayaraman, B., and Anderson, A., "Modeling of Glow Discharge-Induced Fluid Dynamics," *Journal of Applied Physics*, Vol. 92, No. 11, Dec. 2002, pp. 6434–6443.
doi:10.1063/1.1515103

[39] Rizzetta, D. P., and Visbal, M. R., "Numerical Study of Active Flow Control for a Transitional Highly- Loaded Low-Pressure Turbine," *Journal of Fluids Engineering*, Vol. 128, No. 5, Sept. 2006, pp. 956–967.
doi:10.1115/1.2238877

[40] Rizzetta, D. P., and Visbal, M. R., "Numerical Simulation of Separation Control for Transitional Highly-Loaded Low-Pressure Turbines," *AIAA Journal*, Vol. 43, No. 9, Sept. 2005, pp. 1958–1967.
doi:10.2514/1.12376

[41] Beam, R., and Warming, R., "An Implicit Factored Scheme for the Compressible Navier–Stokes Equations," *AIAA Journal*, Vol. 16, No. 4, April 1978, pp. 393–402.
doi:10.2514/3.60901

[42] Gordnier, R. E., and Visbal, M. R., "Numerical Simulation of Delta-Wing Roll," AIAA Paper 1993-0554, Jan. 1993.

[43] Jameson, A., Schmidt, W., and Turkel, E., "Numerical Solutions of the Euler Equations by Finite Volume Methods Using Runge–Kutta Time Stepping Schemes," AIAA Paper 1981-1259, June 1981.

[44] Pulliam, T. H., and Chaussee, D. S., "A Diagonal Form of an Implicit Approximate-Factorization Algorithm," *Journal of Computational Physics*, Vol. 39, No. 2, Feb. 1981, pp. 347–363.
doi:10.1016/0021-9991(81)90156-X

[45] Lele, S. A., "Compact Finite Difference Schemes with Spectral-Like Resolution," *Journal of Computational Physics*, Vol. 103, No. 1, Nov. 1992, pp. 16–42.
doi:10.1016/0021-9991(92)90324-R

[46] Visbal, M. R., and Gaitonde, D. V., "High-Order-Accurate Methods for Complex Unsteady Subsonic Flows," *AIAA Journal*, Vol. 37, No. 10, Oct. 1999, pp. 1231–1239.
doi:10.2514/2.591

[47] Gaitonde, D., Shang, J. S., and Young, J. L., "Practical Aspects of High-Order Accurate Finite-Volume Schemes for Electromagnetics," AIAA Paper 1997-0363, Jan. 1997.

[48] Gaitonde, D., and Visbal, M. R., "High-Order Schemes for Navier–Stokes Equations: Algorithm and Implementation into FDL3DI," U.S. Air Force Research Lab. TR AFRL-VA-WP-TR-1998-3060, Wright-Patterson AFB, OH, Aug. 1998.

[49] Gordnier, R. E., "Computation of Delta-Wing Roll Maneuvers," *Journal of Aircraft*, Vol. 32, No. 3, May 1995, pp. 486–492.
doi:10.2514/3.46746

[50] Visbal, M. R., "Computational Study of Vortex Breakdown on a Pitching Delta Wing," AIAA Paper 1993-2974, July 1993.

[51] Visbal, M., Gaitonde, D., and Gogineni, S., "Direct Numerical Simulation of a Forced Transitional Plane Wall Jet," AIAA Paper 98-2643, June 1998.

[52] Rizzetta, D. P., Visbal, M. R., and Stanek, M. J., "Numerical Investigation of Synthetic-Jet Flowfields," *AIAA Journal*, Vol. 37, No. 8, Aug. 1999, pp. 919–927.
doi:10.2514/2.811

[53] Rizzetta, D. P., and Visbal, M. R., "Direct Numerical Simulation of Flow Past an Array of Distributed Roughness Elements," AIAA Paper 2006-3527, June 2006.

[54] Rizzetta, D. P., and Visbal, M. R., "Numerical Investigation of Transitional Flow Through a Low- Pressure Turbine Cascade," AIAA Paper 2003-3587, June 2003.

[55] Rizzetta, D. P., Visbal, M. R., and Blaisdell, G. A., "A Time-Implicit High-Order Compact Differencing and Filtering Scheme for Large-Eddy Simulation," *International Journal for Numerical Methods in*

Fluids, Vol. 42, No. 6, June 2003, pp. 665–693.
doi:10.1002/fld.551

[56] Rizzetta, D. P., and Visbal, M. R., "Application of Large-Eddy Simulation to Supersonic Compression Ramps," *AIAA Journal*, Vol. 40, No. 8, Aug. 2002, pp. 1574–1581.
doi:10.2514/2.1826

[57] Rizzetta, D. P., and Visbal, M. R., "Large-Eddy Simulation of Supersonic Cavity Flowfields Including Flow Control," *AIAA Journal*, Vol. 41, No. 8, Aug. 2003, pp. 1452–1462.
doi:10.2514/2.2128

[58] Visbal, M. R., and Rizzetta, D. P., "Large-Eddy Simulation on Curvilinear Grids Using Compact Differencing and Filtering Schemes," *Journal of Fluids Engineering*, Vol. 124, No. 4, Dec. 2002, pp. 836–847.
doi:10.1115/1.1517564

[59] Visbal, M. R., Morgan, P. E., and Rizzetta, D. P., "An Implicit LES Approach Based on High-Order Compact Differencing and Filtering Schemes," AIAA Paper 2003-4098, June 2003.

[60] Fureby, C., and Grinstein, F. F., "Monotonically Integrated Large Eddy Simulation," *AIAA Journal*, Vol. 37, No. 5, May 1999, pp. 544–556.
doi:10.2514/2.772

[61] Stoltz, S., and Adams, N. A., "An Approximate Deconvolution Procedure for Large-Eddy Simulation," *Physics of Fluids*, Vol. 11, No. 7, July 1999, pp. 1699–1701.
doi:10.1063/1.869867

[62] Mathew, J., Lechner, R., Foysi, H., Sesterhenn, J., and Friedrich, R., "An Explicit Filtering Method for Large Eddy Simulation of Compressible Flows," *Physics of Fluids*, Vol. 15, No. 8, Aug. 2003, pp. 2279–2289.
doi:10.1063/1.1586271

[63] Steinbrenner, J. P., Chawner, J. P., and Fouts, C. L., "The GRIDGEN 3D Multiple Block Grid Generation System, Volume II: User's Manual," U.S. Air Force Wright Research and Development Center, TR WRDC-TR-90-3022, Wright-Patterson AFB, OH, Feb. 1991.

[64] Visbal, M. R., and Gaitonde, D. V., "Very High-Order Spatially Implicit Schemes for Computational Acoustics on Curvilinear Meshes," *Journal of Computational Acoustics*, Vol. 9, No. 4, Dec. 2001, pp. 1259–1286.
doi:10.1142/S0218396X01000541

[65] Roy, S., and Wang, C.-C., "Bulk Flow Modification with Horseshoe and Serpentine Plasma Actuators," *Journal of Physics D: Applied Physics*, Vol. 42, No. 3, Feb. 2009, Paper 032004.
doi:10.1088/0022-3727/42/3/032004

[66] Katz, A., "Molecular Tagging Velocimetry Measurements of the Low-Reynolds-Number Flow Around an SD7003 Airfoil," M.S. Thesis, Department of Mechanical Engineering, Michigan State Univ., East Lansing, ML, 2010.

[67] Jeong, J., and Hussain, F., "On the Identification of a Vortex," *Journal of Fluid Mechanics*, Vol. 285, Feb. 1995, pp. 69–94.
doi:10.1017/S0022112095000462

A. Naguib
Associate Editor